Misaligned Wind-Waves Behind Atmospheric Cold Fronts

César Sauvage[1], Hyodae Seo[1], Benjamin W. Barr[1], James B. Edson[1], and Carol Anne Clayson[1].

[1]Woods Hole Oceanographic Institution, Woods Hole, Massachusetts, USA

Key Points:

- Passing atmospheric cold fronts generate a large area of growing wind-waves that are misaligned with local wind.
- The misaligned waves increase the roughness length, drag and enthalpy exchange coefficients, and wind stress.
- Representation of the misaligned wave effect in the bulk formula improves the momentum flux estimates.

Corresponding author: César Sauvage, csauvage@whoi.edu

Abstract

Atmospheric fronts embedded in extratropical cyclones are high-impact weather phenomena, contributing significantly to midlatitude winter precipitation. The three vital characteristics of the atmospheric fronts, high wind speeds, abrupt change in wind direction, and rapid translation, force the induced surface waves to be misaligned with winds exclusively behind the cold fronts. The effects of the misaligned waves on air-sea fluxes remain undocumented. Using the multi-year in situ near-surface observations and direct covariance flux measurements from the Pioneer Array off the coast of New England, we find that the majority of the passing cold fronts generate misaligned waves behind the cold front. Once generated, the waves remain misaligned, on average, for about 8 hours. The fully-coupled model simulations indicate that the misaligned waves significantly increase the roughness length (300%), drag coefficient (30%), and momentum flux (20%). The increased surface drag reduces the wind speeds in the surface layer. The upward turbulent heat flux is weakly decreased by the misaligned waves because of the compensating effect between the decrease in temperature and humidity scaling parameters and the increase in friction velocity. The misaligned wave effect is not accurately represented in a commonly used wave-based bulk flux algorithm. Yet, the suggested modification to the current formulation improves the overall accuracy of parameterized momentum flux estimates. The results imply that better representing a directional wind-wave coupling in the bulk formula of the numerical models may help improve the air-sea interaction simulations under the passing atmospheric fronts in the midlatitudes.

Plain Language Summary

Atmospheric fronts are recurrent weather phenomena in midlatitudes, significantly contributing to winter precipitation. They are characterized by high wind speeds, abrupt change in wind direction, and rapid translation. Their passage over the ocean lead to the generation of strongly misaligned waves, particularly behind the cold fronts. The effects of these misaligned waves on air-sea fluxes remain undocumented. Using the long term surface observations from the Pioneer Array off the coast of New England, we find that the majority of the passing atmospheric fronts generate misaligned waves behind the cold front which can remain misaligned, on average, for about 8 hours. The use of coupled numerical experiments indicate that the misaligned waves significantly increase the ocean roughness length and momentum flux, which reduce the surface wind speeds.

The misaligned wave effect is not accurately represented in a commonly used wave based air-sea flux algorithm. Yet, the suggested modification to the current formulation improves the overall accuracy of parameterized momentum flux estimates. The results imply that better representing a directional wind-wave coupling in numerical models may help improve the air-sea interaction simulations under the passing atmospheric fronts in the midlatitudes.

1 Introduction

Air-sea momentum, heat, and moisture exchanges are mediated by interactions between near-surface atmospheric turbulence and the ocean surface wave field. Wave fields are complex and may include contributions from a wide range of frequencies and directions, including strongly coupled short wind-waves with wavelengths of O(0.1-10 m) and frequencies higher than twice the spectral peak (Phillips, 1966; Makin et al., 1995; Kukulka & Hara, 2005), developing to mature locally generated wind-waves and remotely generated long-period swell. In many current modern sea state-dependent (or wave-based) bulk flux algorithms, the surface waves that determine the surface drag are often assumed to be in the direction of winds. However, there are many wind and wave regimes where this assumption is not valid and where using it can yield notable deficiencies in the parameterized momentum flux. Swell waves under the low-wind condition (Grachev & Fairall, 2001; G. Chen et al., 2002; Hanley & Belcher, 2008; Hanley et al., 2010; Sullivan et al., 2008) or the mixed seas under the trade wind (Sauvage et al., 2023) or tropical cyclones (S. S. Chen et al., 2013; Reichl et al., 2014; S. S. Chen & Curcic, 2016; Hsu et al., 2019; X. Chen et al., 2020) are well-known examples in the lower-latitudes. Existing studies suggest a complex relationship between wind-wave misalignment and surface stress, which may be regime-dependent (e.g., high winds in tropical cyclones vs. lower winds in midlatitudes). For instance, Zhou et al. (2022) found that misalignment between local winds and tropical cyclone-generated swell reduced the drag coefficient in high winds, suggesting quadrant-specific variations in drag due to storm-scale misalignment patterns. On the other hand, Porchetta et al. (2019) examined in situ observations from the North Sea and the U.S. New England coast and found that wind-wave misalignment increases the surface drag, with additional influence by wave age.

In the midlatitudes, the atmospheric fronts are embedded in the extratropical cyclones and significantly modulate the day-to-day weather variability. They feature elon-

gated along-frontal scales of 1000s km comparable to the lateral extent of the extratropical cyclones, but much shorter cross-frontal scales of 10-100 km (Figure 1, Bjerknes & Solberg, 1922). Figure 1a shows a typical extratropical cyclone we will examine in this study. Traveling rapidly eastward at ≈10 m/s, the atmospheric fronts accompany gale-force near-surface winds (15-30 m/s), which also abruptly shift in direction from the southerly in the warm sector to the northwesterly in the cold sector. Although atmospheric fronts typically occur 10-30% in the wintertime North Atlantic (Hewson, 1998; Berry et al., 2011; Parfitt et al., 2017; Reeder et al., 2021), they are known to contribute to up to 90% of the precipitation (Catto & Pfahl, 2013; Soster & Parfitt, 2022), often in an extreme form (Catto & Pfahl, 2013) and, hence, they are one of the most important high-impact weather phenomena in the midlatitudes. Interactions between the cold airmass of the fronts and the warmer ocean (and ocean fronts) via air-sea turbulent heat fluxes influence the intensity of these events (Parfitt et al., 2016; Seo et al., 2023). The atmospheric cold fronts are also known to force significant surges and complex wave reactions that severely impact coastal and estuary circulations and wetland evolutions (Kim et al., 2020; Cao et al., 2020; Guo et al., 2020). However, their impacts on surface drag and momentum flux in the midlatitudes are undocumented in the literature. We will demonstrate that directional wave-wind coupling can modulate these surface fluxes, impacting the surface drag and near-surface winds.

The three crucial characteristics of the atmospheric fronts relevant to misaligned waves are high winds, abrupt changes in wind direction, and rapid translation. In the warm sector of the fronts, the strong southerly winds force the strongly coupled short wind-waves, generally aligned with the winds. Once the cold front is crossed, the marked shift in the wind direction, combined with the rapid eastward translation, generates a large fetch of growing wind-waves that become quickly misaligned with the northwesterly winds. Figure 1b illustrates this process schematically. Here, we define that the waves are misaligned with winds when the propagation direction of the most dominant wave differs from the wind direction by $>60°$. Not only is this definition intuitive, but it is also consistent with the observed changes in directional wave spreading across the cold front (not shown).

This study identifies and examines the evolutions of misaligned waves under atmospheric fronts using direct in-situ surface flux measurements and fully-coupled high-resolution ocean-atmosphere-wave model simulations. A possible modification to more accurately

represent the relevant wave-wind physics in the bulk flux parameterization is also discussed. Section 2 describes the observations, parameterizations, and model simulations. Section 3 provides a case study investigation of misaligned waves for one atmospheric front case using model simulations and observations, while Section 4 offers the climatological perspectives of the evolution of misaligned waves and their impacts on parameterized flux using observations. Section 5 concludes the study.

2 Methods

2.1 Observations

The Pioneer Array, located off the coast of New England and operated by the NSF Ocean Observatories Initiative (OOI, Trowbridge et al., 2019), provides various meteorological and ocean observations of physical, chemical, and biological processes from December 2014 until November 2022. This study uses the 8-years of near-surface measurements of wind, temperature, humidity, and surface wave fields. We also use the momentum fluxes from the direct covariance flux system (DCFS), available over a shorter period (2015-05-13 - 2015-10-23; 2016-05-13 - 2018-03-29; 2018-10-30 - 2019-04-07). NOAA's National Data Buoy Center (NDBC) buoys off the New England coast are also used, especially surface wave information, including 2D wave spectrum along with significant wave height, dominant wave period, and mean/peak wave direction, co-located with the near-surface measurements of winds, temperature, humidity, pressure, and ocean surface temperature.

2.2 SCOAR coupled regional modeling system

We use the Scripps Coupled Ocean-Atmosphere Regional model (SCOAR, Seo et al., 2007, 2014, 2016, 2021; Sauvage et al., 2023), which couples the Weather Research and Forecast model (WRF, Skamarock et al., 2019) in the atmosphere to the Regional Ocean Modeling System (ROMS, Haidvogel et al., 2000; Shchepetkin & McWilliams, 2005) in the ocean and WAVEWATCH III (WW3, Tolman et al., 2002; The WAVEWATCH III Development Group, 2019) for the surface waves. ROMS is driven by the momentum, heat, and freshwater fluxes parameterized from COARE3.5 (Fairall et al., 1996, 2003; Edson et al., 2013) implemented in the WRF Mellor-Yamada-Nakanishi-Niino (MYNN) surface layer scheme (Nakanishi & Niino, 2009; Jiménez et al., 2012). ROMS forces WRF

by feeding SST and surface current vectors to the WRF surface layer scheme. Between WRF and WW3, the model offers various wave-to-atmosphere coupling options to determine the surface fluxes, as documented in detail in Sauvage et al. (2023). This study will examine two particular wave-based roughness length formulations, as described in Section 2.3. ROMS provides surface current to WW3 to represent the current effect on waves. WW3 can also be coupled to ROMS to represent energy dissipation due to wave-breaking and whitecapping. However, the WW3-ROMS coupling is not considered in this study.

2.3 Momentum flux parameterizations

The momentum flux (τ), sensible (H_s) and latent (H_l) heat fluxes are parameterized via COARE (Fairall et al., 1996) as:

$$\tau = \rho_a C_D S_r U_r = \rho_a u_*^2, \tag{1}$$

$$H_s = \rho_a C_{pa} C_h S_r \Delta T = -\rho_a C_{pa} u_* T_*, \tag{2}$$

$$H_l = \rho_a L_e C_e S_r \Delta Q = -\rho_a L_e u_* q_*, \tag{3}$$

where ρ_a is the air density, C_{pa} is the specific heat capacity of the air at constant pressure, L_e is the latent heat of evaporation, T is the potential temperature, Q is the water vapor mixing ratio, S_r is the scalar averaged wind speed relative to the ocean surface, U_r is the magnitude of the wind vector relative to the ocean surface, C_D, C_h, C_e are the transfer coefficients for stress, sensible and latent heat, and u_*, T_*, q_* are the Monin-Obukhov similarity scaling parameters. The drag coefficient C_D is defined as:

$$C_D(z, z_0, \psi_m) = \left[\frac{\kappa}{ln(z/z_0) - \psi_m(\zeta)}\right]^2, \tag{4}$$

where κ is the von Kármán constant, $\psi_m(\zeta)$ is an empirical function of atmospheric stability, ζ is the z/L ratio with L the Obukhov length and z the height above the surface. The COARE wave-based formulation (Edson et al., 2013) parameterizes the wave-induced surface roughness (z_0^{rough}, hereafter simply z_0) as,

$$z_0 = H_s D(\frac{u_*}{c_p})^B, \tag{5}$$

where H_s is the significant wave height, u_*/c_p is the inverse wave age based on u_* , and the peak phase speed of the wave (c_p). D and B are numerical constants given by $D =$

0.09 and $B = 2$ (Edson et al., 2013). In addition to Eq. 5 included in the COARE3.5 public release, Sauvage et al. (2023) tested a revised formulation, in which z_0 increases as the wave-wind misalignment increases (Porchetta et al., 2019, 2021),

$$z_0 = H_s D cos(a\theta)(\frac{u_*}{c_p})^{Bcos(b\theta)}, \tag{6}$$

where θ is the absolute directional difference between the 10-m wind and the peak wave direction. D and B are the same coefficients as in Eq. 5, while the coefficients $a = 0.45$ and $b = -0.32$ are determined by Porchetta et al. (2019) from a set of midlatitude offshore in situ measurements, including the Air-Sea Interaction Tower (ASIT) south of Martha's Vineyard, which is close to the region of the current study.

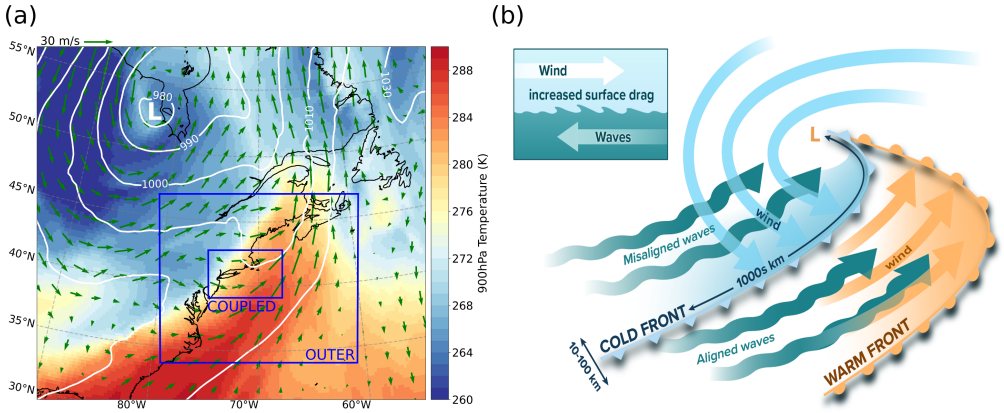

Figure 1. (a) An extratropical cyclone in the North Atlantic on December 6, 2017, at 12:00 UTC, showing the potential temperature at 900 hPa (K), overlaid with the mean sea level pressure (contours, hPa) and the 900 hPa wind (arrows), from the ERA5 reanalysis. The extent of the outer and nested model domains is also indicated. (b) A schematic representation of an atmospheric front passing over the ocean showing aligned wind-waves under the warm sector and strongly misaligned waves behind the cold front. The schematic at the top left represents the mechanism of the enhanced drag behind the cold front when wind and waves are misaligned. The "L" symbol denotes the center of the low-pressure system in both (a,b).

2.4 Experiments

The model domain covers the North Atlantic (Figure 1a) with a nested configuration. In the outer domain, the model is run at 7.5 km resolution and is atmosphere-only, dynamically downscaling the large-scale atmospheric circulation with spectral nudg-

ing. This drives the inner domain zooming over the US Northeast (Figure 1a), where WRF, ROMS, and WW3 are fully coupled at an hourly frequency and run at the identical 1.5 km resolution with matching grids and land-sea masks. ROMS has 30 vertical levels with a stretched vertical grid that enables the enhanced resolutions near the surface and the bottom, with $\theta_s = 7.0$, $\theta_b = 0.1$, and h_{cline}= 300 m, yielding a minimum of 15 layers in the upper 150 m. The vertical resolution of WRF is refined to have 50 vertical levels with ≈20 levels below 250 m. The lowest level is close to the surface (5. 5m), with the 2nd lowest level at 12 m per Shin et al. (2012).

In WRF, deep cumulus convection is represented through the Multi-scale Kain-Fritsch scheme (Zheng et al., 2016), the cloud micro-physics by the WRF single-moment 6-class scheme (Hong & Lim, 2006), the land surface process by the Noah land surface model (F. Chen & Dudhia, 2001), and the Rapid Radiative Transfer Model for general circulation models (RRTMG, Iacono et al., 2008) for the shortwave and longwave radiations. The planetary boundary layer (PBL) processes are treated with the MYNN level 2.5 scheme (Nakanishi & Niino, 2009). In ROMS, the KPP (K profile parameterization) scheme (Large et al., 1994) determines vertical eddy viscosity and diffusivity. In WW3, the ST6 package is used to parameterize wind input, wave breaking, and swell dissipation (Babanin, 2011; Stopa et al., 2016; Liu et al., 2019). Nonlinear wave–wave interactions are computed using the discrete interaction approximation (Hasselmann et al., 1985). Reflection by shorelines is enabled through the Ardhuin and Roland (2012) scheme. The depth-induced breaking is based on Battjes and Janssen (1978), and the bottom friction formulation follows Ardhuin et al. (2003).

Two coupled model simulations are run for a 3-day case study (December 5-8, 2017) featuring one passing atmospheric front (Figure 1a). In the simulation dubbed $WBF\theta$, the roughness length is parameterized by Eq. 6, where the wind and wave misalignment effect is considered. This will be compared to another simulation, called WBF, where such an effect is omitted (Eq. 5). In both simulations, the WRF model is initialized and driven by the 1-hr 0.25° ERA5 reanalysis (Hersbach et al., 2020), ROMS by the daily 1/12° MERCATOR International global reanalysis (Lellouche et al., 2018), and WW3 by 11 spectral points obtained from the global 1/2° WW3 simulations (Rascle & Ardhuin, 2013). The initial conditions for WW3 were obtained from the 30-day spin-up simulations forced by ERA5 atmospheric forcing. In ROMS, the tidal forcing is obtained using the Oregon State University Tidal Prediction Software (Egbert & Erofeeva, 2002)

and applied as a 2-D open boundary condition by prescribing the tidal period, elevation amplitude, current phase angle, current inclination angle, the minimum, and maximum tidal current, and ellipse semi-minor axes for 13 major tidal constituents (Steffen et al., 2023).

3 Case Study Examination

This section uses in situ observations and model simulations to examine the misaligned waves during one atmospheric front. To provide spatial context, we will discuss the model results first. Figure 2 compares three stages of a cold front passage, showing the directional misalignment (θ) and the wind-speed-based wave age ($\chi = c_p/U_{10}$) for three different times: December 6 at 09:00 UTC, when the Pioneer Array is ahead of the cold front (pre-cold-front), at 12:00 UTC (cold-front), and at 15:00 UTC (post-cold-front). Hereafter, U_{10} is defined as $U_{10} = (U_{10x}^2 + U_{10y}^2)^{1/2}$ where U_{10x} is the zonal and U_{10y} is the meridional wind components.

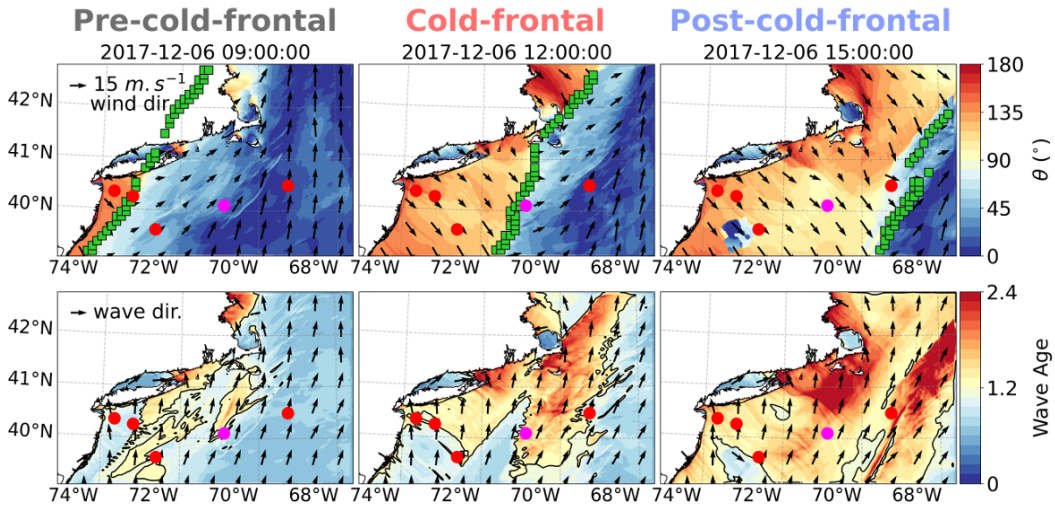

Figure 2. The top row shows the evolution of θ (shading), overlaid with the surface wind (black arrows) as simulated from the WBFθ run at 09:00 (pre-cold-front), 12:00 (cold-front) and 15:00 (post-cold-front) UTC on December 6, 2017. The green markers indicate the detected cold front using the Parfitt et al. (2017) algorithm. The bottom row shows the evolution of the wave age, overlaid with the wave peak direction (normalized black arrows). A wave age of 1.2 is indicated by a black contour. The magenta circle denotes the location of the Pioneer Array, and the 4 red circles are the NDBC moorings (from left to right: mooring identification numbers 44065, 44025, 44066, and 44008).

3.1 Evolutions of winds and waves

During the pre-cold-front, the directional misalignment is generally small ($\theta < 45°$). The strong southerly and southwesterly wind (black vectors in the top row) in the warm sector is associated with the southerly waves (black vectors in the bottom row), with an overall developing sea state ($\chi < 1.2$). The wind abruptly switches to northwesterly across the cold front. In response, strongly misaligned waves with $\theta > 100°$ occur over a broad fetch west of the cold front, with χ rising above 1.2. As the front moves eastward, a new area of misaligned waves is continuously generated in the far east, with the developing sea state ($\chi < 1.2$) progressively turning into a mixed sea state ($1.2 < \chi < 3$) in the far west. Much of the sea state behind the cold front is a mixture of two wave categories: slightly older southerly wind waves forced by the warm sector southerly wind and newly generated younger short wind waves forced by the cold sector northwesterly wind (Figures 2 and 3).

These wind and wave evolutions from the model are consistent with the observations at the Pioneer Array. Figure 3 shows the hourly time series of the near-surface meteorological and wave measurements. During the pre-cold-front (gray-shaded period), southerly winds (black arrows) with >10 m/s and a developing sea state ($\chi \leq 1.2$) were observed. The waves were largely aligned with the wind (red arrows). After the cold front passage on December 6 at 12:00 UTC (red-shaded period), the near-surface air temperature and relative humidity dropped rapidly, and the wind direction switched to northwesterly, while the dominant wave direction continued to be southerly, indicating a large degree of wave-wind misalignment ($\theta \geq 100°$) and a mixed sea state ($\chi > 1.2$). For this particular event, the wind waves remained misaligned with the winds for more than 18 hours after the cold front, after which the waves gradually became aligned with the wind, and the wave age subsided below 1.2.

The adjacent NDBC buoys captured similar wave responses. The 2D wave spectra plots constructed from the 4 NDBC buoys (Figure 4) indicate that during the pre-cold-front, the dominant wave direction is southerly, with wave periods of 5-10s. Even after the cold front passes, these southerly surface waves persist, while new short waves with a period lower than 5s are generated from the northwest. While there is a reasonable range of regional variability across the buoys, the salient feature of the wave responses is broadly consistent across all the buoys examined. Compared to the Pioneer Array and

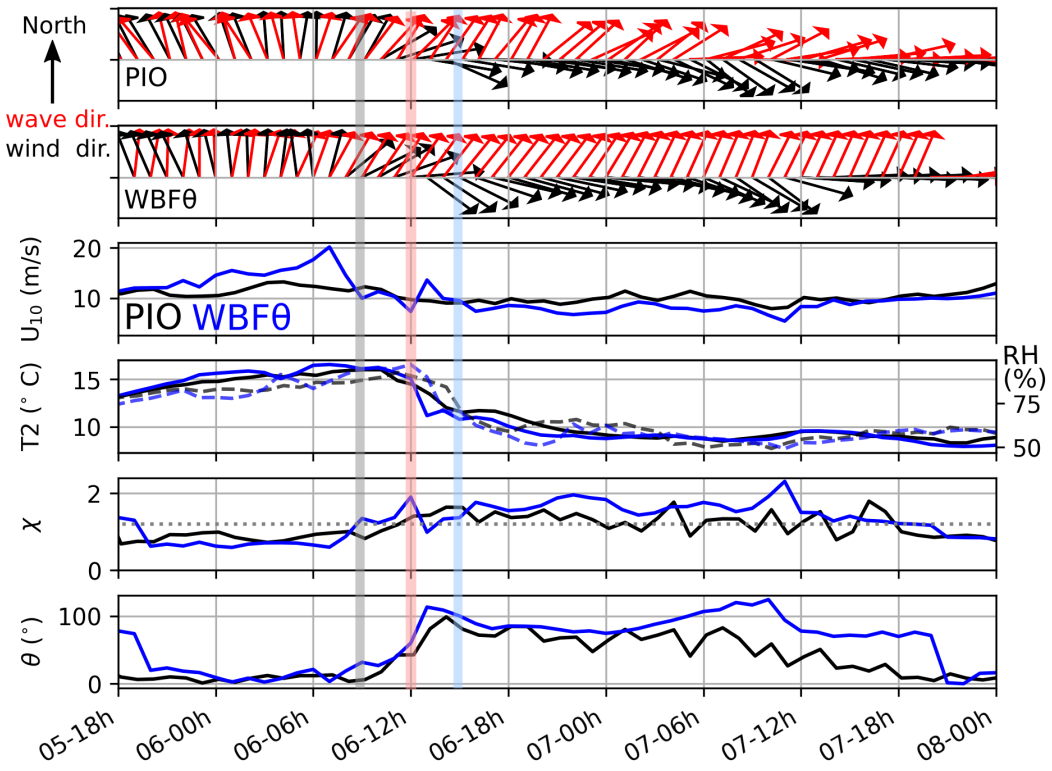

Figure 3. The top two panels show the observed and simulated (WBFθ) wind direction (black arrows) and wave peak direction (red arrows) around the passing of the atmospheric front on December 6, 2017. The length of the arrows in the top two panels is normalized. Gray, red, and blue shaded periods denote the pre-cold-front, cold-front, and post-cold-front shown in Figure 2. The following panels show the 10 m wind speed (U_{10}, m/s), air temperature (T2, solid line, °C), relative humidity (RH, dashed line, %), wave age, and misalignment angle (θ, °) from the Pioneer Array (black) and WBFθ (blue). The dotted gray line on the wave age panel denotes the wave age = 1.2.

the NDBC buoys, the simulation (WBFθ) also captures the characteristics of the atmospheric front and the observed wave evolution reasonably well. The model also captures the background easterly swell observed from the NDBC buoys.

Figure 5 shows the frequency-averaged wave energy density spectra (E_f) during the passage of the atmospheric front in WBFθ. The top row shows the average energy coming from the 90° sectors from the southwest to southeast direction, while the bottom row shows the energy coming from the 90° sectors from the west to north direction. Strong southerly wave energy builds under the warm sector ahead of the cold front and

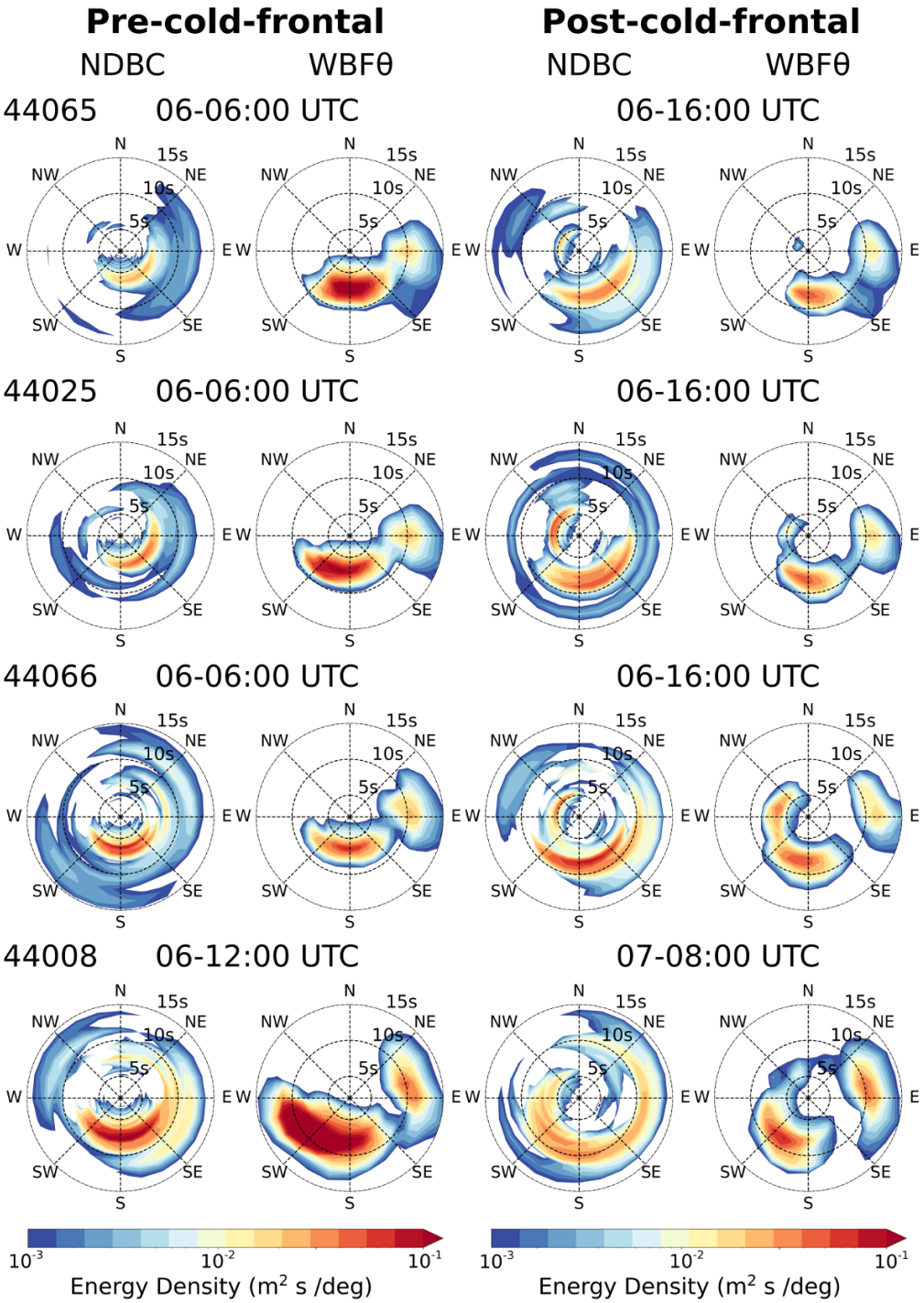

Figure 4. The 2D wave energy density spectra ($m^2 s/°$) shown in the period space calculated from the 4 NDBC mooring locations, 44065, 44025, 44066, and 4408 (see Figure 2 for mooring locations) and the WBFθ run during a pre-cold-front (left column) and post-cold-front (right column) time.

dissipates as the cold front passes over the region. Meanwhile, the northwesterly winds behind the cold front generate new waves coming from the northwest, so the wave energy from that direction grows following the cold front, creating mixed sea conditions. Note that the color scale on Figure 5 is different on both rows and indicates that the southerly energy is much stronger and dominant even after the cold front, leading to the observed wind and wave misalignment. As suggested in Figure 3, more than 18 hours after the passage of the cold front is needed for the waves to be aligned again and for the southerly wave energy under the warm sector to dissipate eventually.

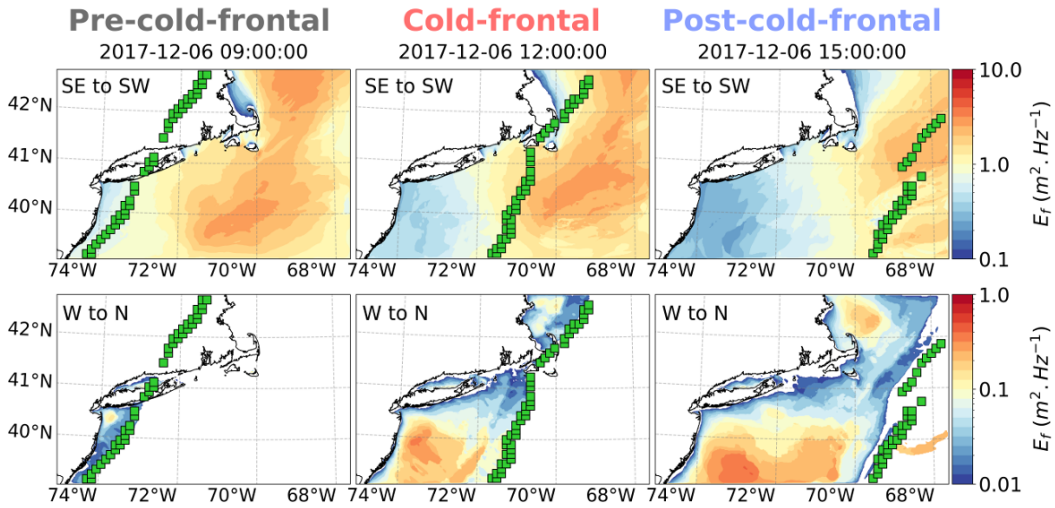

Figure 5. The frequency-averaged wave energy density spectra (E_f, $m^2.Hz^{-1}$) as simulated from the WBFθ run at 09:00 (pre-cold-front), 12:00 (cold-front) and 15:00 (post-cold-front) UTC on December 6, 2017. The green markers indicate the detected cold front using the Parfitt et al. (2017) algorithm. The top row shows the energy coming from the 90° sector from the southeast to southwest direction (SE to SW), while the bottom row shows the energy coming from the 90° sector from the west to north direction (W to N).

3.2 Impacts on surface drag and momentum flux

The WBFθ run is compared with the WBF run to reveal the effect of misaligned waves. For this, we will focus on differences in directly impacted variables: z_0, C_D, τ, and wind speeds at two different heights, 10 m (within the surface layer, U_{10}) and 110 m (above the surface layer, U_{110}). We will also discuss the changes in turbulent heat flux

after that. For simplicity, we will compare the difference only at the post-cold-front (December 6, 15:00 UTC).

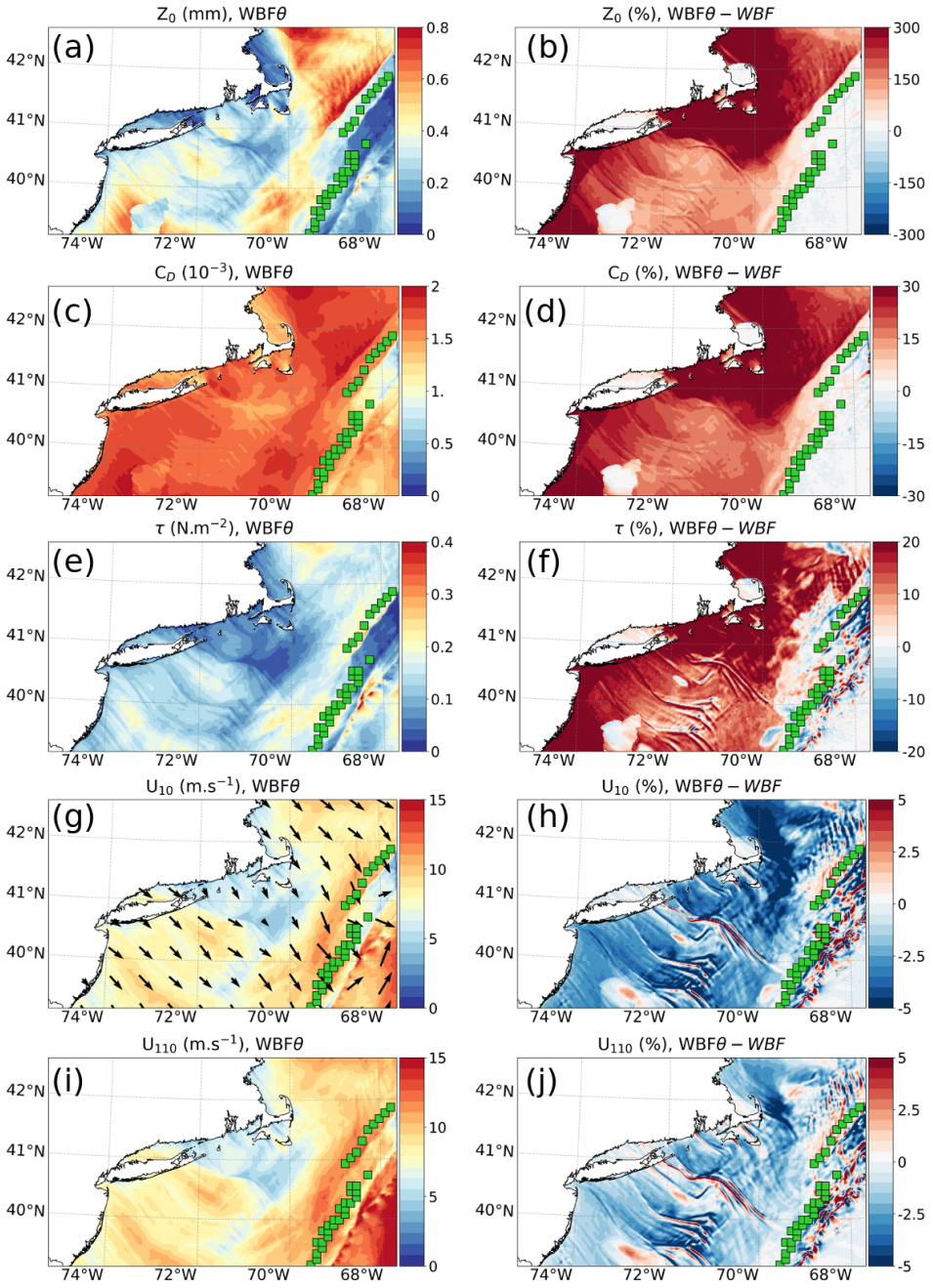

Figure 6. (a,c,e,g,i) shows the roughness length (z_0), drag coefficient (C_D), momentum flux (τ), surface wind speed (U_{10}) and wind speed at 110 m (U_{110}) from WBFθ and (b,d,f,h,j) the percent difference between WBFθ and WBF (%) after the passage of the cold front, at 15:00 UTC on December 6, 2017. The arrows overlaid on U_{10} indicate the direction of the surface wind. The green markers indicate the detected cold front using the Parfitt et al. (2017) algorithm.

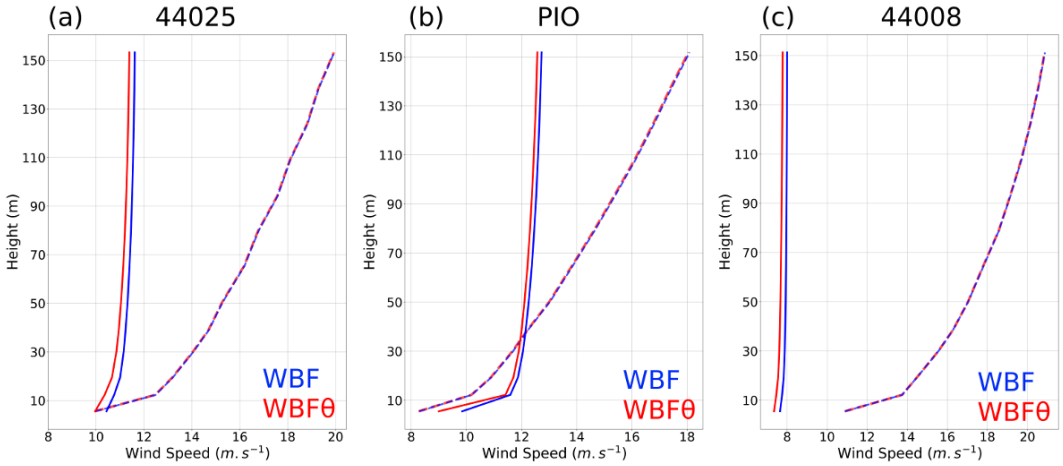

Figure 7. Vertical wind speed profiles from WBF (blue) and WBFθ (red) at (b) Pioneer Array location and (a,c) two NDBC moorings, 44025 and 44008. On each plot, a profile before (dashed) and a profile after (solid) the passage of the cold front is shown. For NDBC moorings (a,c), the times are chosen to be the same as in Figure 4, while for Pioneer Array (b), the times are chosen to be the pre-cold-front and post-cold-front shown in Figure 2.

The left column of Figure 6 shows WBFθ, and the right column shows the difference between WBFθ and WBF, expressed as the percentage difference ((WBFθ - WBF) / WBF) $\times$100). East of the cold front, where the wave and wind are largely aligned, little difference is found in each of these four quantities. However, sizable increases are found in z_0, C_D, and τ west of the cold front. The increase can be as high as 300% for z_0, 30% for C_D, and 20% for τ, respectively. If area-averaged over the broad region west of the cold front, the increases are 185.7%, 19.3%, and 11%, respectively (Fig. 6a-d). Moreover, because of the increase in the surface drag, U_{10} is reduced in WBFθ by up to 5% (or 2% when area-averaged, Fig. 6g,h). The increased drag by the misaligned wave is also felt above the surface layer. Here, the wind at 110 m is chosen to show the impact above the surface layer (Figure 6i,j). U_{110} is reduced behind the cold front, having a coherent spatial pattern to that of U_{10}. However, the magnitude of the reduction above the surface layer is generally small (1-5% or 0.1-0.5 m.s^{-1}, Figure 6i,j). Figure 7 shows wind speed profiles at different NDBC moorings and Pioneer Array locations, confirming that the effect of increased drag by the misaligned waves on wind speed is largest in the surface layer and smaller above it.

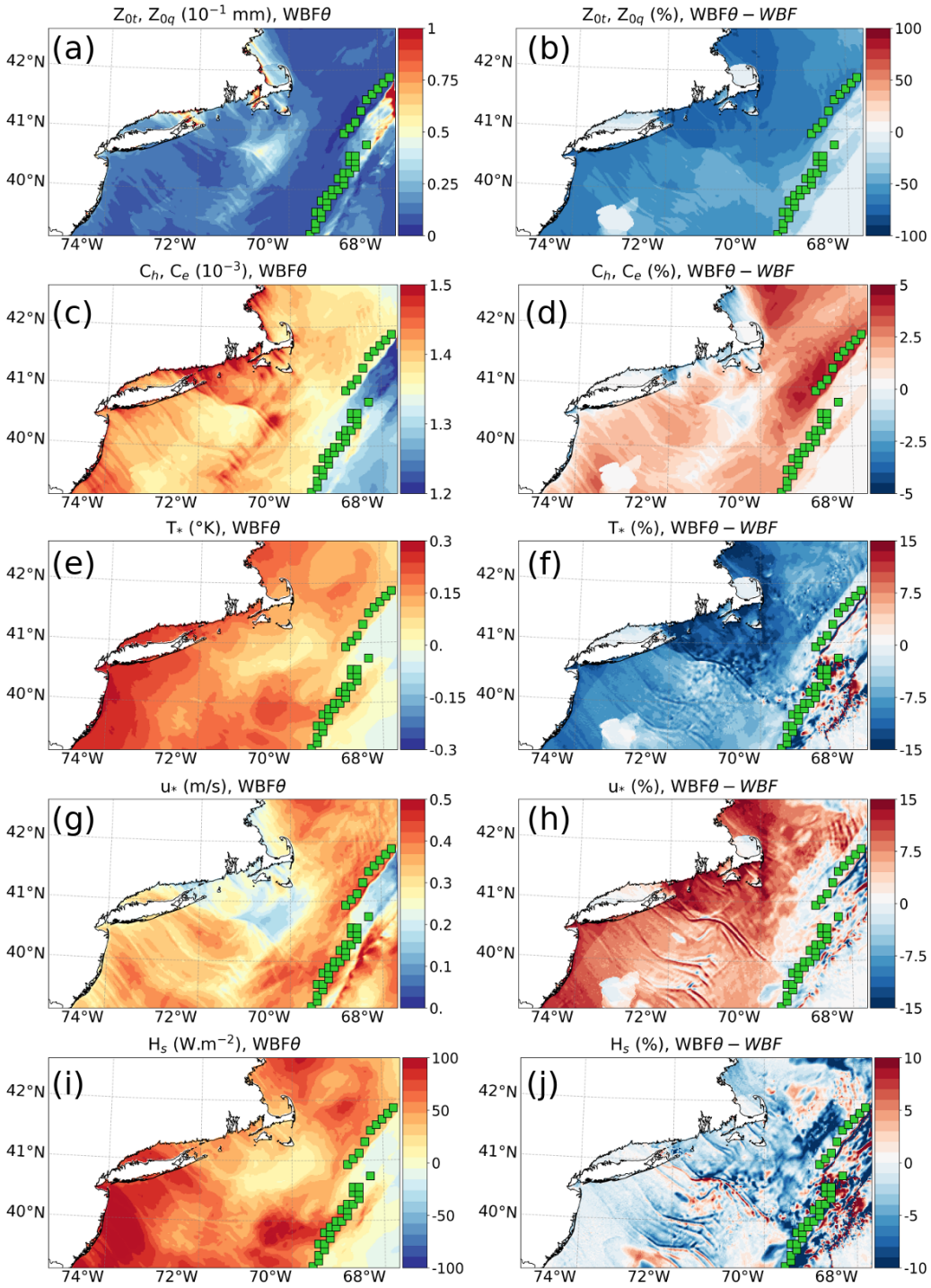

Figure 8. As in Figure 6, but for the scalar roughness length (z_{0t}, z_{0q}, $10^{-1}mm$), the exchange coefficient for heat and moisture (C_h, C_e, 10^{-3}), the temperature scaling parameter (T_*, $^\circ K$), the friction velocity (u_*, m.s^{-1}) and the sensible heat flux (H_s, $W.m^{-2}$). Heat flux is defined as positive upward.

3.3 Impacts on turbulent heat flux

The increases in surface roughness length due to misaligned waves also modify the upward sensible heat flux (H_s) and latent heat flux (H_l), reducing them west of the cold front by up to 10% (2.5% when area-averaged, Figure 8i,j and Figure 9c,d). This decrease in upward turbulent heat fluxes occurs despite a moderate increase in the exchange coefficients for heat and moisture (respectively C_h and C_e; note that these are equal in the COARE3.5 algorithm) by up to 5% (Figure 8c,d). To investigate in more detail the impact on heat fluxes, based on WRF outputs from WBF and WBFθ and using COARE3.5 offline, we re-calculated the scalar roughness length for temperature and humidity (z_{0t} and z_{0q}), the surface exchange coefficients (C_h and C_e) and the specific humidity scaling parameter (q_*) which are not directly given by WRF outputs. Comparing the implementation of COARE3.5 in the MYNN surface scheme (Olson et al., 2021) to the COARE3.5 offline version, we are confident that the result would be the same if taken directly from WRF. z_{0t} is defined using the roughness Reynolds number (R_r) as:

$$R_r = \frac{u_* z_0}{\nu}, \tag{7}$$

$$z_{0t} = \frac{5.8e^{-5}}{R_r^{0.72}}, \tag{8}$$

where ν is the kinematic viscosity of the air. In COARE3.5, the moisture roughness length z_{0q} is equal to z_{0t}. The sensible and latent heat transfer coefficients are defined as

$$C_h(z, z_0, z_{0t}, \psi_m, \psi_h) = \left[\frac{\kappa}{ln(z/z_0) - \psi_m(\zeta)}\right]\left[\frac{\kappa}{ln(z/z_{0t}) - \psi_h(\zeta)}\right], \tag{9}$$

$$C_e(z, z_0, z_{0q}, \psi_m, \psi_h) = \left[\frac{\kappa}{ln(z/z_0) - \psi_m(\zeta)}\right]\left[\frac{\kappa}{ln(z/z_{0q}) - \psi_h(\zeta)}\right], \tag{10}$$

where $\psi_h(\zeta)$ is another empirical function of atmospheric stability. Because $z_{0q} = z_{0t}$ in COARE3.5, $C_e = C_h$.

The scalar roughness length z_{0t} is inversely proportional to the velocity roughness length z_0, so an increase in z_0 due to wave misalignment (Fig. 6a,b) drives a decrease in z_{0t} (60% when area-averaged, Figure 8a,b). This increased resistance to turbulent scalar transport decreases the magnitude of the turbulent flux scale for temperature, T_*, by up

to 15%, Figure 8e,f. Note that T_* and the turbulent moisture flux scale q_* are defined to be negative for heat fluxes out of the ocean, so we plot $-T_*$ and $-q_*$ so that positive values of these quantities correspond to positive values of H_s and H_l. Overall, in Eq. 2, the increase in u^* due to misalignment (Figure 8g,h) is more than offset by the decrease in $-T_*$, resulting in a small decrease in sensible heat flux. Similarly, the decrease in z_{0q} induces a decrease in $-q_*$, which compensates for the increase in u_* and results in a small decrease in H_l overall, Equation 3 and Figure 9.

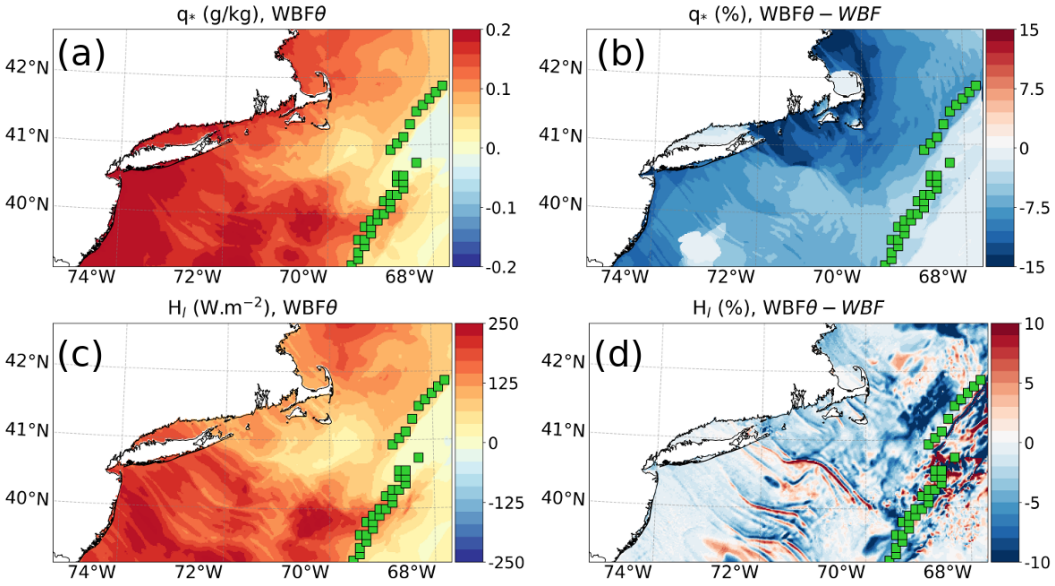

Figure 9. As in Figure 6 but for (a,b) the specific humidity scaling parameter (q_*, g/kg) and (c,d) the latent heat flux (H_l, $W.m^{-2}$).

4 Long-term characterization

Multi-year measurements of near-surface meteorology, surface waves, and direct covariance fluxes from the Pioneer Array are used to examine the long-term characteristics of the misaligned waves under cold fronts. To do that, we first have to detect the cold front from the buoys. Because surface-based observations are used, the detected fronts can be deemed surface cold fronts. Here, we use the meridional surface wind (U_{10y}) and the 2-m air temperature (T2). The cold front is identified when U_{10y} is shifted from southerly to northerly, with an additional criterion that the northerly (southerly) U_{10y} must persist over 2 hrs after (before) the frontal passage. We then check for a decrease in T2 by >3°C between t=-2 hrs and t=+8 hrs. To ensure a strong shift in wind direction at the

passage of the cold front, we also require a change in wind direction of at least 60°. If all these conditions are met, the event is considered an atmospheric cold front over the Pioneer Array at t=0. Using this set of criteria, 86 atmospheric cold fronts were identified from the 8-year Pioneer Array dataset. 55 of these events have co-located measurements of surface waves, which are used for subsequent analysis. Hereafter, we defined misaligned waves when the angle between wind and waves exceeds at least 60°. The results presented here do not change appreciably with reasonable variations of criteria.

Figure 10a shows the histogram of the so-detected cold front occurrence as a function of calendar months. Consistent with the previous studies (Parfitt et al., 2017; Reeder et al., 2021), the cold fronts are most frequently observed during the extended winter period (November - March), with 62 out of 86 events. Figure 10b shows the composite evolutions of θ across the fronts, indicating strongly misaligned waves at the cold front passage (t=0).

These fronts feature southerly wind (Figure 10c) with moderate speed (8 m/s, Figure 10d) in the warm sector accompanied by a strong shift in wind direction from the warm to cold sectors exceeding at least 60° (Figure 10c). Because of moderate wind conditions in the warm sector, the sea state is generally characterized by a mixed sea ($1.2< \chi <2$), where wind-waves and some pre-existing swell co-exist, the condition that was also observed from the NDBC buoys (Figure 4). As the cold front passes and the winds change direction, the waves begin to be misaligned 1$\sim$2 hrs before the front, and once generated, the waves remain misaligned for 8 hours on average (Figure 10b).

We use the DCFS momentum flux measurements at the Pioneer Array to evaluate the accuracy of the parameterized momentum flux. Because DCFS data are available for a shorter period (see Section 2.1), only 36 atmospheric front events were identified from this period, of which 20 have led to misaligned waves ($\theta > 60°$). Figure 11a,b shows the composite evolutions of the directly measured C_d and τ (black) for the fronts that generated the misaligned waves. With the state variables measured from the Pioneer Array, we then calculated C_d and τ without misaligned waves (blue, Eq. 5) and with misaligned waves (red, Eq. 6). The result shows that the estimated momentum flux with misaligned waves is higher than without by 16.5% at t=0 and 6.6% for 8 hours after the cold front. When averaged over the 8 hours after the cold front, this elevated wind stress with misaligned waves is closer to the DCFS estimates (bias is reduced from 4.9%

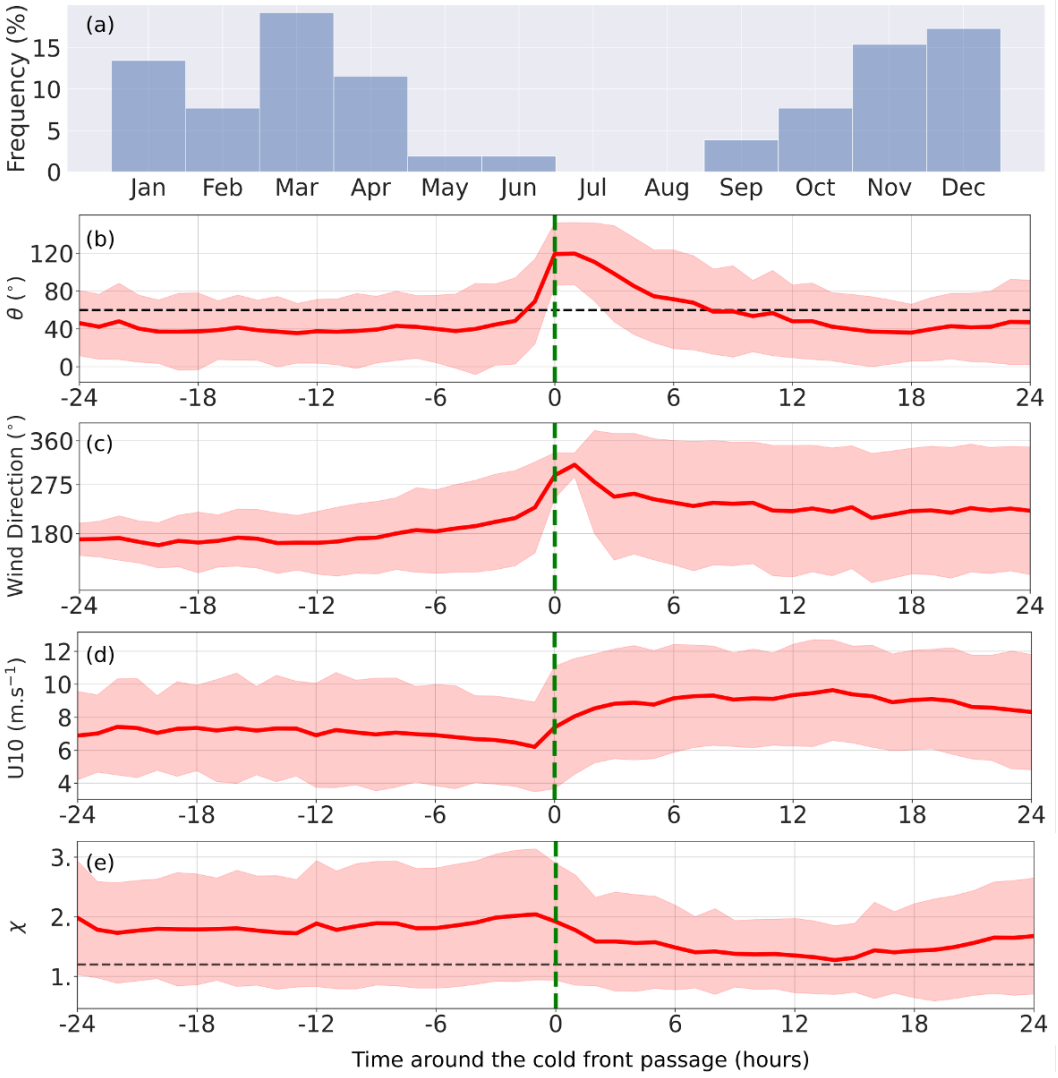

Figure 10. (a) Probability of occurrence of cold front per month (%) calculated using the Pioneer Array data from December 2014 to November 2022. (b,c,d,e) Composite evolutions of (b) misalignment angle (θ, °), (c) wind direction (°, 0 means northerly), (d) wind speed (m/s), and (e) wave age for the detected atmospheric cold fronts. The shaded envelopes represent ± 1 standard deviations. In (b), the dashed line indicates the 60° line; in (e), a wave age 1.2. The vertical green line indicates the cold front a t=0.

to 1.1% for τ and from 6% to 1.1% for C_d). The results also corroborate the modeling results (WBF vs. WBFθ).

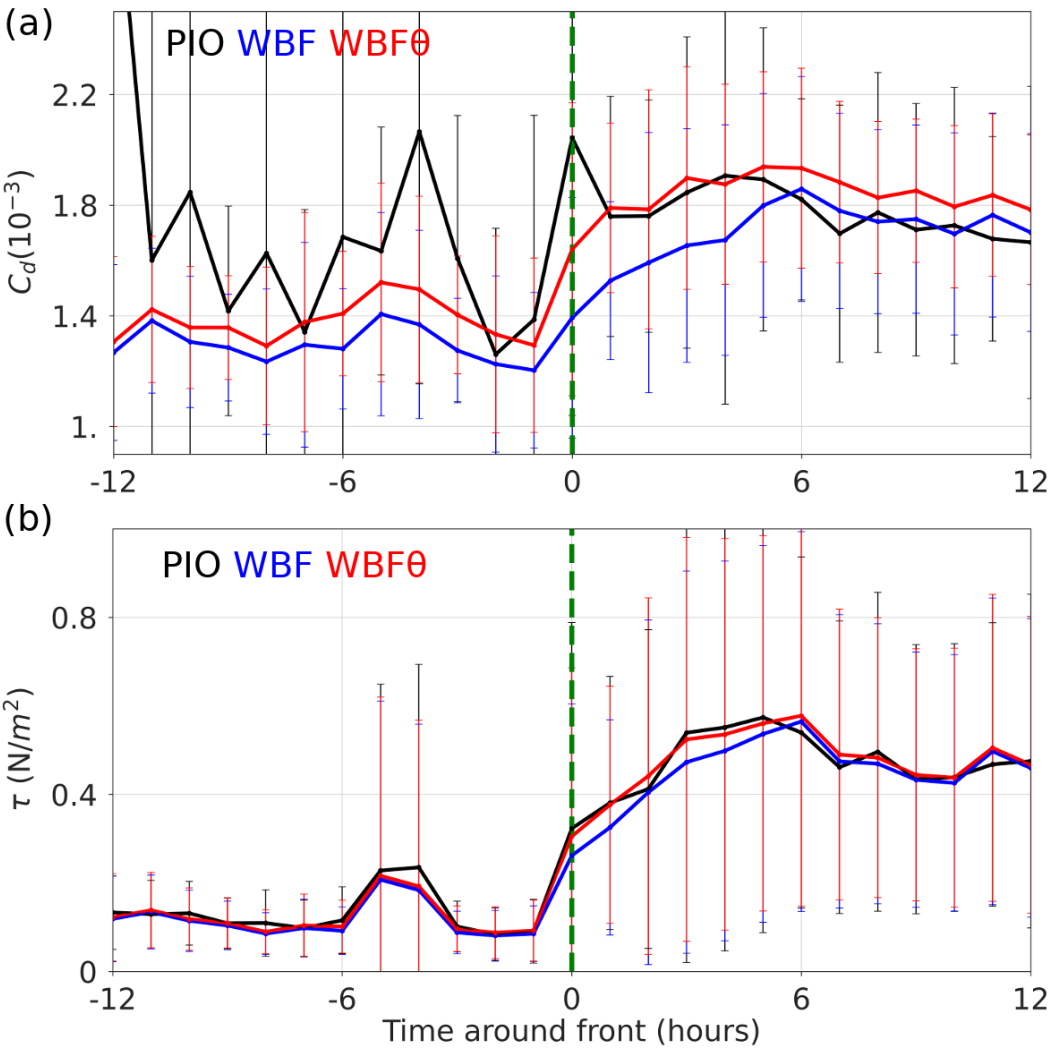

Figure 11. Composite evolution of the parameterized (a) drag coefficient ($C_d, 10^{-3}$) and (b) momentum flux (τ, Nm^{-2}) calculated offline using the COARE3.5 (WBFθ, red) with and (WBF, blue) without the misaligned wave effect, in comparison to direct covariance flux measurements from the Pioneer Array (PIO, black). The error bars represent ± 1 standard deviation. The vertical green line indicates the cold front a t=0.

5 Conclusion and Discussions

Using the multi-year in-situ observations and numerical model simulations, this study examined the nature and impacts of the misaligned surface waves behind the passing of atmospheric cold fronts off the coast of New England. A case study investigation indicates that an atmospheric cold front generates a significant fetch of misaligned waves behind it, comparable to the lateral extent of the extratropical cyclones in which the front

is embedded. Over a vast region of misaligned waves propagating with the front, the model simulations indicate that misaligned waves significantly increase the roughness length, drag and enthalpy exchange coefficients, and wind stress. In response to increased surface drag, the near-surface wind speed is reduced, reducing upward turbulent heat fluxes. Note that the decrease in upward turbulent heat flux is despite the moderate increase in surface heat and moisture exchange coefficients. Indeed, the scalar roughness decreased as the velocity roughness increased, decreasing the temperature and humidity scaling parameters and increasing the friction velocity. This leads to compensating effects on both latent and sensible heat fluxes. Hence, the magnitudes of the responses in turbulent heat fluxes are modest.

The long-term analysis using the Pioneer Array data allowed us to detect over 50 atmospheric cold fronts, which generated misaligned waves behind them. Once generated, these waves remain misaligned with the wind for 8 hours on average. This percentage of atmospheric cold front detection, of course, depends on the chosen threshold, but the results are qualitatively similar.

The current COARE wave-based bulk flux parameterization assumes that waves and wind are aligned (Eq. 5). A simple modification to this formulation is suggested to represent the misaligned wave effect as in Eq. (6), which produces overall improved estimates of the parameterized momentum flux under this condition. As discussed extensively in Sauvage et al. (2023), equivalent to incorporating the directional misalignment in COARE is simply replacing the peak wave period with the mean wave period to calculate the wave age in Eq. (5) (See their Eq. 12). The rationale is that the spectrally-averaged wave period more accurately depicts a sea state that is a mixture of wind waves of ranging frequencies, as in Figure 4.

Finally, the impacts of the improved surface stress on the wind profile appear limited to the surface layer. An important caveat to consider is that the present analysis mainly concerns the "instantaneous" impacts of the altered momentum flux, whereas, in the nature and long-term coupled runs, the mixed layer depth will likely respond to different turbulent momentum and heat fluxes, thereby greatly affecting state variables such as sea surface temperature. These effects cannot be captured in the short 3-day simulations. Longer simulations that fully resolve the interactions between the atmospheric fronts and surface waves are needed to determine the impacts on kinematic and ther-

modynamic properties in the PBL and upper ocean and possibly the evolution of the atmospheric fronts.

6 Open Research

ERA5 data are made available by Copernicus Climate Change Service (`https://cds.climate.copernicus.eu`), Mercator by Copernicus Marine Environment Monitoring Service (`https://doi.org/10.48670/moi-00016`), and global 3-hourly spectral wave analyses by Ifremer (ftp://ftp.ifremer.fr/ifremer/ww3/HINDCAST/GLOBAL). OOI Pioneer Array data are obtained from `https://dataexplorer.oceanobservatories.org`, and NDBC data from `!https://www.ndbc.noaa.gov/`. WW3 is distributed via `https://github.com/NOAA-EMC/WW3`, WRF `https://github.com/wrf-model/WRF`, and ROMS `!https://www.myroms.org/`. The SCOAR codes are available via `https://github.com/SCOAR-model/SCOAR`. The modified COARE3.5 code is available at `https://github.com/cesarsauvage/COARE3.5_modified_Sauvage-et-al._2023` and the model outputs at `Zenodo`.

Acknowledgments

This research was supported by NOAA (NA19OAR4310376), NASA (80NSSC21K1524), NSF (OCE-2148120), and DOE (DE-EE0009424). Additionally, HS acknowledges NSF (OCE-2022846). The WHOI High-Performance Computing Facility provided the computing resources.

References

Ardhuin, F., O'Reilly, W. C., Herbers, T. H. C., & Jessen, P. F. (2003). Swell Transformation across the Continental Shelf. Part I: Attenuation and Directional Broadening. *Journal of Physical Oceanography*, *33*(9), 1921–1939. doi: 10.1175/1520-0485(2003)033⟨1921:STATCS⟩2.0.CO;2

Ardhuin, F., & Roland, A. (2012). Coastal wave reflection, directional spread, and seismoacoustic noise sources. *Journal of Geophysical Research: Oceans*, *117*(C11). doi: 10.1029/2011JC007832

Babanin, A. (2011). *Breaking and Dissipation of Ocean Surface Waves*. Cambridge: Cambridge University Press. doi: 10.1017/CBO9780511736162

Battjes, J. A., & Janssen, J. P. F. M. (1978). Energy Loss and Set-Up Due to Breaking of Random Waves. *Coastal Engineering*, 569–587. doi: 10.1061/9780872621909.034

Berry, G., Reeder, M. J., & Jakob, C. (2011). A global climatology of atmospheric fronts. *Geophysical Research Letters*, *38*(4). doi: 10.1029/2010GL046451

Bjerknes, J., & Solberg, H. (1922). Life of the Cyclones and the Polar Front Theory of Atmospheric Circulation. *Geophysisks Publikationer*, *3*(1), 18.

Cao, Y., Li, C., & Dong, C. (2020). Atmospheric Cold Front-Generated Waves in the Coastal Louisiana. *Journal of Marine Science and Engineering*, *8*(11), 900. doi: 10.3390/jmse8110900

Catto, J. L., & Pfahl, S. (2013). The importance of fronts for extreme precipitation. *Journal of Geophysical Research: Atmospheres*, *118*(19), 10,791–10,801. doi: 10.1002/jgrd.50852

Chen, F., & Dudhia, J. (2001). Coupling an Advanced Land Surface–Hydrology Model with the Penn State–NCAR MM5 Modeling System. Part I: Model Implementation and Sensitivity. *Monthly Weather Review*, *129*(4), 569–585. doi: 10.1175/1520-0493(2001)129⟨0569:CAALSH⟩2.0.CO;2

Chen, G., Chapron, B., Ezraty, R., & Vandemark, D. (2002). A Global View of Swell and Wind Sea Climate in the Ocean by Satellite Altimeter and Scatterometer. *Journal of Atmospheric and Oceanic Technology*, *19*(11), 1849–1859. doi: 10.1175/1520-0426(2002)019⟨1849:AGVOSA⟩2.0.CO;2

Chen, S. S., & Curcic, M. (2016). Ocean surface waves in Hurricane Ike (2008) and Superstorm Sandy (2012): Coupled model predictions and observations. *Ocean*

Modelling, *103*, 161–176. doi: 10.1016/j.ocemod.2015.08.005

Chen, S. S., Zhao, W., Donelan, M. A., & Tolman, H. L. (2013). Directional Wind–Wave Coupling in Fully Coupled Atmosphere–Wave–Ocean Models: Results from CBLAST-Hurricane. *Journal of the Atmospheric Sciences*, *70*(10), 3198–3215. doi: 10.1175/JAS-D-12-0157.1

Chen, X., Ginis, I., & Hara, T. (2020). Impact of Shoaling Ocean Surface Waves on Wind Stress and Drag Coefficient in Coastal Waters: 2. Tropical Cyclones. *Journal of Geophysical Research: Oceans*, *125*(7), e2020JC016223. doi: 10.1029/2020JC016223

Edson, J. B., Jampana, V., Weller, R. A., Bigorre, S. P., Plueddemann, A. J., Fairall, C. W., ... Hersbach, H. (2013). On the Exchange of Momentum over the Open Ocean. *Journal of Physical Oceanography*, *43*(8), 1589–1610. doi: 10.1175/JPO-D-12-0173.1

Egbert, G. D., & Erofeeva, S. Y. (2002). Efficient Inverse Modeling of Barotropic Ocean Tides. *Journal of Atmospheric and Oceanic Technology*, *19*(2), 183–204. doi: 10.1175/1520-0426(2002)019⟨0183:EIMOBO⟩2.0.CO;2

Fairall, C. W., Bradley, E. F., Hare, J. E., Grachev, A. A., & Edson, J. B. (2003). Bulk Parameterization of Air–Sea Fluxes: Updates and Verification for the COARE Algorithm. *Journal of Climate*, *16*(4), 571–591. doi: 10.1175/1520-0442(2003)016⟨0571:BPOASF⟩2.0.CO;2

Fairall, C. W., Bradley, E. F., Rogers, D. P., Edson, J. B., & Young, G. S. (1996). Bulk parameterization of air-sea fluxes for Tropical Ocean-Global Atmosphere Coupled-Ocean Atmosphere Response Experiment. *Journal of Geophysical Research: Oceans*, *101*(C2), 3747–3764. doi: 10.1029/95JC03205

Grachev, A. A., & Fairall, C. W. (2001). Upward Momentum Transfer in the Marine Boundary Layer. *Journal of Physical Oceanography*, *31*(7), 1698–1711. doi: 10.1175/1520-0485(2001)031⟨1698:UMTITM⟩2.0.CO;2

Guo, B., Subrahmanyam, M. V., & Li, C. (2020). Waves on Louisiana Continental Shelf Influenced by Atmospheric Fronts. *Scientific Reports*, *10*(1), 272. doi: 10.1038/s41598-019-55578-w

Haidvogel, D. B., Arango, H. G., Hedstrom, K., Beckmann, A., Malanotte-Rizzoli, P., & Shchepetkin, A. F. (2000). Model evaluation experiments in the North Atlantic Basin: Simulations in nonlinear terrain-following co-

ordinates. *Dynamics of Atmospheres and Oceans*, *32*(3), 239–281. doi: 10.1016/S0377-0265(00)00049-X

Hanley, K. E., & Belcher, S. E. (2008). Wave-Driven Wind Jets in the Marine Atmospheric Boundary Layer. *Journal of the Atmospheric Sciences*, *65*(8), 2646–2660. doi: 10.1175/2007JAS2562.1

Hanley, K. E., Belcher, S. E., & Sullivan, P. P. (2010). A Global Climatology of Wind–Wave Interaction. *Journal of Physical Oceanography*, *40*(6), 1263–1282. doi: 10.1175/2010JPO4377.1

Hasselmann, S., Hasselmann, K., Allender, J. H., & Barnett, T. P. (1985). Computations and Parameterizations of the Nonlinear Energy Transfer in a Gravity-Wave Specturm. Part II: Parameterizations of the Nonlinear Energy Transfer for Application in Wave Models. *Journal of Physical Oceanography*, *15*(11), 1378–1391. doi: 10.1175/1520-0485(1985)015⟨1378:CAPOTN⟩2.0.CO;2

Hersbach, H., Bell, B., Berrisford, P., Hirahara, S., Horányi, A., Muñoz-Sabater, J., ... Thépaut, J.-N. (2020). The ERA5 global reanalysis. *Quarterly Journal of the Royal Meteorological Society*, *146*(730), 1999–2049. doi: 10.1002/qj.3803

Hewson, T. D. (1998). Objective fronts. *Meteorological Applications*, *5*(1), 37–65. doi: 10.1017/S1350482798000553

Hong, S.-Y., & Lim, J.-O. J. (2006). The WRF Single-Moment 6-Class Microphysics Scheme (WSM6). *JOURNAL OF THE KOREAN METEOROLOGICAL SOCIETY*.

Hsu, J.-Y., Lien, R.-C., D'Asaro, E. A., & Sanford, T. B. (2019). Scaling of Drag Coefficients Under Five Tropical Cyclones. *Geophysical Research Letters*, *46*(6), 3349–3358. doi: 10.1029/2018GL081574

Iacono, M. J., Delamere, J. S., Mlawer, E. J., Shephard, M. W., Clough, S. A., & Collins, W. D. (2008). Radiative forcing by long-lived greenhouse gases: Calculations with the AER radiative transfer models. *Journal of Geophysical Research: Atmospheres*, *113*(D13). doi: 10.1029/2008JD009944

Jiménez, P. A., Dudhia, J., González-Rouco, J. F., Navarro, J., Montávez, J. P., & García-Bustamante, E. (2012). A Revised Scheme for the WRF Surface Layer Formulation. *Monthly Weather Review*, *140*(3), 898–918. doi: 10.1175/MWR-D-11-00056.1

Kim, J.-Y., Kaihatu, J., Chang, K.-A., Sun, S.-H., Huff, T. P., & Feagin, R. A.

(2020). Effect of Cold Front-Induced Waves Along Wetlands Boundaries. *Journal of Geophysical Research: Oceans*, *125*(12), e2020JC016603. doi: 10.1029/2020JC016603

Kukulka, T., & Hara, T. (2005). Momentum flux budget analysis of wind-driven air-water interfaces. *Journal of Geophysical Research: Oceans*, *110*(C12). doi: 10.1029/2004JC002844

Large, W. G., McWilliams, J. C., & Doney, S. C. (1994). Oceanic vertical mixing: A review and a model with a nonlocal boundary layer parameterization. *Reviews of Geophysics*, *32*(4), 363–403. doi: 10.1029/94RG01872

Lellouche, J.-M., Greiner, E., Le Galloudec, O., Garric, G., Regnier, C., Drevillon, M., ... Le Traon, P.-Y. (2018). Recent updates to the Copernicus Marine Service global ocean monitoring and forecasting real-time 1/12° high-resolution system. *Ocean Science*, *14*(5), 1093–1126. doi: 10.5194/os-14-1093-2018

Liu, Q., Rogers, W. E., Babanin, A. V., Young, I. R., Romero, L., Zieger, S., ... Guan, C. (2019). Observation-Based Source Terms in the Third-Generation Wave Model WAVEWATCH III: Updates and Verification. *Journal of Physical Oceanography*, *49*(2), 489–517. doi: 10.1175/JPO-D-18-0137.1

Makin, V. K., Kudryavtsev, V. N., & Mastenbroek, C. (1995). Drag of the sea surface. *Boundary-Layer Meteorology*, *73*(1), 159–182. doi: 10.1007/BF00708935

Nakanishi, M., & Niino, H. (2009). Development of an Improved Turbulence Closure Model for the Atmospheric Boundary Layer. *Journal of the Meteorological Society of Japan. Ser. II*, *87*(5), 895–912. doi: 10.2151/jmsj.87.895

Olson, J. B., Smirnova, T., Kenyon, J. S., Turner, D. D., Brown, J. M., Zheng, W., & Green, B. W. (2021). A Description of the MYNN Surface-Layer Scheme. *NOAA Technical Memorandum OAR GSL*. doi: 10.25923/F6A8-BC75

Parfitt, R., Czaja, A., Minobe, S., & Kuwano-Yoshida, A. (2016). The atmospheric frontal response to SST perturbations in the Gulf Stream region. *Geophysical Research Letters*, *43*(5), 2299–2306. doi: 10.1002/2016GL067723

Parfitt, R., Czaja, A., & Seo, H. (2017). A simple diagnostic for the detection of atmospheric fronts. *Geophysical Research Letters*, *44*(9), 4351–4358. doi: 10.1002/2017GL073662

Phillips, O. M. (1966). *The Dynamics of the Upper Ocean*. Cambridge U.P.

Porchetta, S., Temel, O., Muñoz-Esparza, D., Reuder, J., Monbaliu, J., Van Beeck,

J., & Van Lipzig, N. (2019). A new roughness length parameterization accounting for wind–wave (mis)alignment. *Atmospheric Chemistry and Physics*, *19*(10), 6681–6700. doi: 10.5194/acp-19-6681-2019

Porchetta, S., Temel, O., Warner, J., Muñoz-Esparza, D., Monbaliu, J., Van Beeck, J., & Van Lipzig, N. (2021). Evaluation of a roughness length parametrization accounting for wind–wave alignment in a coupled atmosphere–wave model. *Quarterly Journal of the Royal Meteorological Society*, *147*(735), 825–846. doi: 10.1002/qj.3948

Rascle, N., & Ardhuin, F. (2013). A global wave parameter database for geophysical applications. Part 2: Model validation with improved source term parameterization. *Ocean Modelling*, *70*, 174–188. doi: 10.1016/j.ocemod.2012.12.001

Reeder, M. J., Spengler, T., & Spensberger, C. (2021). The Effect of Sea Surface Temperature Fronts on Atmospheric Frontogenesis. *Journal of the Atmospheric Sciences*, *78*(6), 1753–1771. doi: 10.1175/JAS-D-20-0118.1

Reichl, B. G., Hara, T., & Ginis, I. (2014). Sea state dependence of the wind stress over the ocean under hurricane winds. *Journal of Geophysical Research: Oceans*, *119*(1), 30–51. doi: 10.1002/2013JC009289

Sauvage, C., Seo, H., Clayson, C. A., & Edson, J. B. (2023). Improving Wave-Based Air-Sea Momentum Flux Parameterization in Mixed Seas. *Journal of Geophysical Research: Oceans*, *128*(3), e2022JC019277. doi: 10.1029/2022JC019277

Seo, H., Miller, A. J., & Norris, J. R. (2016). Eddy–Wind Interaction in the California Current System: Dynamics and Impacts. *Journal of Physical Oceanography*, *46*(2), 439–459. doi: 10.1175/JPO-D-15-0086.1

Seo, H., Miller, A. J., & Roads, J. O. (2007). The Scripps Coupled Ocean–Atmosphere Regional (SCOAR) Model, with Applications in the Eastern Pacific Sector. *Journal of Climate*, *20*(3), 381–402. doi: 10.1175/JCLI4016.1

Seo, H., O'Neill, L. W., Bourassa, M. A., Czaja, A., Drushka, K., Edson, J. B., ... Wang, Q. (2023). Ocean Mesoscale and Frontal-Scale Ocean–Atmosphere Interactions and Influence on Large-Scale Climate: A Review. *Journal of Climate*, *36*(7), 1981–2013. doi: 10.1175/JCLI-D-21-0982.1

Seo, H., Song, H., O'Neill, L. W., Mazloff, M. R., & Cornuelle, B. D. (2021). Impacts of ocean currents on the South Indian Ocean extratropical storm

track through the relative wind effect. *Journal of Climate*, 1–61. doi: 10.1175/JCLI-D-21-0142.1

Seo, H., Subramanian, A. C., Miller, A. J., & Cavanaugh, N. R. (2014). Coupled Impacts of the Diurnal Cycle of Sea Surface Temperature on the Madden–Julian Oscillation. *Journal of Climate*, *27*(22), 8422–8443. doi: 10.1175/JCLI-D-14-00141.1

Shchepetkin, A. F., & McWilliams, J. C. (2005). The regional oceanic modeling system (ROMS): A split-explicit, free-surface, topography-following-coordinate oceanic model. *Ocean Modelling*, *9*(4), 347–404. doi: 10.1016/j.ocemod.2004.08.002

Shin, H. H., Hong, S.-Y., & Dudhia, J. (2012). Impacts of the Lowest Model Level Height on the Performance of Planetary Boundary Layer Parameterizations. *Monthly Weather Review*, *140*(2), 664–682. doi: 10.1175/MWR-D-11-00027.1

Skamarock, C., Klemp, B., Dudhia, J., Gill, O., Liu, Z., Berner, J., ... Huang, X.-y. (2019). A Description of the Advanced Research WRF Model Version 4.1. *(No. NCAR/TN-556+STR)*. doi: 10.5065/1dfh-6p97

Soster, F., & Parfitt, R. (2022). On Objective Identification of Atmospheric Fronts and Frontal Precipitation in Reanalysis Datasets. *Journal of Climate*, *35*(14), 4513–4534. doi: 10.1175/JCLI-D-21-0596.1

Steffen, J., Seo, H., Clayson, C. A., Pei, S., & Shinoda, T. (2023). Impacts of tidal mixing on diurnal and intraseasonal air-sea interactions in the Maritime Continent. *Deep Sea Research Part II: Topical Studies in Oceanography*, *212*, 105343. doi: 10.1016/j.dsr2.2023.105343

Stopa, J. E., Ardhuin, F., Babanin, A., & Zieger, S. (2016). Comparison and validation of physical wave parameterizations in spectral wave models. *Ocean Modelling*, *103*, 2–17. doi: 10.1016/j.ocemod.2015.09.003

Sullivan, P. P., Edson, J. B., Hristov, T., & McWilliams, J. C. (2008). Large-Eddy Simulations and Observations of Atmospheric Marine Boundary Layers above Nonequilibrium Surface Waves. *Journal of the Atmospheric Sciences*, *65*(4), 1225–1245. doi: 10.1175/2007JAS2427.1

The WAVEWATCH III Development Group, W. (2019). *User manual and system documentation of WAVEWATCH III R© version 6.07* (Tech. Note 333). College Park, MD, USA,: NOAA/NWS/NCEP/MMAB,.

Tolman, H. L., Balasubramaniyan, B., Burroughs, L. D., Chalikov, D. V., Chao, Y. Y., Chen, H. S., & Gerald, V. M. (2002). Development and Implementation of Wind-Generated Ocean Surface Wave Modelsat NCEP. *Weather and Forecasting*, *17*(2), 311–333. doi: 10.1175/1520-0434(2002)017⟨0311:DAIOWG⟩2.0.CO;2

Trowbridge, J., Weller, R., Kelley, D., Dever, E., Plueddemann, A., Barth, J. A., & Kawka, O. (2019). The Ocean Observatories Initiative. *Frontiers in Marine Science*, *6*.

Zheng, Y., Alapaty, K., Herwehe, J. A., Genio, A. D. D., & Niyogi, D. (2016). Improving High-Resolution Weather Forecasts Using the Weather Research and Forecasting (WRF) Model with an Updated Kain–Fritsch Scheme. *Monthly Weather Review*, *144*(3), 833–860. doi: 10.1175/MWR-D-15-0005.1

Zhou, X., Hara, T., Ginis, I., D'Asaro, E., Hsu, J.-Y., & Reichl, B. G. (2022). Drag Coefficient and Its Sea State Dependence under Tropical Cyclones. *Journal of Physical Oceanography*, *52*(7), 1447–1470. doi: 10.1175/JPO-D-21-0246.1